

# N-Type Surface Design for p-Type CZTSSe Thin Film to Attain High Efficiency

Yali Sun, Pengfei Qiu, Wei Yu, Jianjun Li, Hongling Guo, Li Wu, Hao Luo, Rutao Meng, Yi Zhang,\* and Shengzhong (Frank) Liu\*

As a low-cost substitute that uses no expensive rare-earth elements for the high-efficiency  $\text{Cu}(\text{In,Ga})(\text{S,Se})_2$  solar cell, the  $\text{Cu}_2\text{ZnSn}(\text{S,Se})_4$  (CZTSSe) solar cell has borrowed optimization strategies used for its predecessor to improve its device performance, including a profiled band gap and surface inversion. Indeed, there have been few reports of constructing CZTSSe absorber layers with surface inversion to improve efficiency. Here, a strategy that designs the CZTSSe absorber to attain surface modification by using n-type  $\text{Ag}_2\text{ZnSnS}_4$  is demonstrated. It has been discovered that Ag plays two major roles in the kesterite thin film devices: surface inversion and front gradient distribution. It has not only an excellent carrier transport effect and reduced probability of electron-hole recombination but also results in increased carrier separation by increasing the width of the depletion region, leading to much improved  $V_{\text{OC}}$  and  $J_{\text{SC}}$ . Finally, a champion CZTSSe solar cell renders efficiency as high as 12.55%, one of the highest for its type, with the open-circuit voltage deficit reduced to as low as 0.306 V (63.2% Shockley-Queisser limit). The band engineering for surface modification of the absorber and high efficiency achieved here shine a new light on the future of the CZTSSe solar cell.

ment of CZTSSe is a large open-circuit voltage deficit ( $V_{\text{OC,def}}$ ). Many optimization strategies borrowed from CIGSSe solar cells have been used to break through the current high  $V_{\text{OC,def}}$  issue of CZTSSe materials, including isovalent cation doping<sup>[5–11]</sup> and gradient band-gap design.<sup>[12]</sup> Ag is equivalent to Cu but its ion radius is larger than that of Cu, which will reduce the recombination caused by the high density of Cu/Zn antisite defects, thereby reducing  $V_{\text{OC,def}}$ .<sup>[5,13]</sup> Simultaneously, Ag doping can enlarge the band gap ( $E_g$ ) of the absorber layer, which will be effective for increasing the open voltage ( $V_{\text{OC}}$ ) of thin film photovoltaic devices.<sup>[12,14–17]</sup> Based on the above advantages of Ag doping, our group prepared Ag-doped  $(\text{Ag,Cu})_2\text{ZnSnSe}_4$  solar cells through pre-alloying followed by a selenization process, and the  $V_{\text{OC}}$  of the devices was improved.<sup>[12]</sup>

## 1. Introduction

The  $\text{Cu}_2\text{ZnSn}(\text{S,Se})_4$  (CZTSSe) thin film solar cell, which has similar material properties and device structure as  $\text{Cu}(\text{In,Ga})(\text{S,Se})_2$  (CIGSSe), has received great attention because of its benign and rich elemental composition and excellent photovoltaic characteristics. Currently, the highest conversion efficiency has exceeded 12.6%, but this is still much lower than that of CIGSSe.<sup>[1–4]</sup> A major bottleneck restricting the develop-

There is, however, a problem with incorporating Ag into kesterite film, i.e., Ag diffuses very quickly and easily distributes uniformly throughout the whole absorber film during the high temperature annealing process. Therefore it is difficult to control the content along the depth of CZTSSe films.<sup>[14,18]</sup> Theoretical calculations and experimental results both show that  $\text{Ag}_2\text{ZnSn}(\text{S,Se})_4$  is an n-type material and can form a p–n junction with CZTSSe,<sup>[13,15,19]</sup> but it cannot ensure the existence of n-type  $(\text{Cu,Ag})_2\text{ZnSn}(\text{S,Se})_4$  on the surface due to the quick diffusion of Ag. So far, surface type

Y. Sun, H. Guo, R. Meng, Y. Zhang  
 Institute of Photoelectronic Thin Film Devices and Technology  
 of Nankai University  
 Tianjin Key Laboratory of Thin Film Devices and Technology  
 Engineering Research Center of Thin Film Photoelectronic  
 Technology  
 Tianjin 300350, China  
 E-mail: yizhang@nankai.edu.cn  
 P. Qiu, W. Yu, H. Luo  
 College of Physics Science and Technology  
 Hebei University  
 Baoding 071002, China

The ORCID identification number(s) for the author(s) of this article can be found under <https://doi.org/10.1002/adma.202104330>.

DOI: 10.1002/adma.202104330

J. Li  
 Australian Centre for Advanced Photovoltaics  
 School of Photovoltaic and Renewable Energy Engineering  
 University of New South Wales  
 Sydney, NSW 2052, Australia  
 L. Wu  
 Key Laboratory of Weak-Light Nonlinear Photonics Ministry of Education  
 School of Physics  
 Nankai University  
 Tianjin 300071, China  
 S. (F.) Liu  
 Key Laboratory of Applied Surface and Colloid Chemistry  
 National Ministry of Education Institute for Advanced Energy Materials  
 School of Materials Science and Engineering  
 Shaanxi Normal University  
 Xi'an 710119, China  
 E-mail: liusz@snnu.edu.cn

inversion, an excellent strategy to promote the efficiency of CIGSSe solar cells greatly,<sup>[20,21]</sup> is still a huge challenge for the kesterite solar cell.

In this work, we successfully overcome the challenge of fast diffusion of Ag in kesterite film and realize an n-type surface on the p-type CZTSSe thin film by a novel Ag-doping strategy. The devices with such an n-type surface not only have excellent hole blocking on the surface of the absorber layer to reduce the recombination of the heterojunction interface but also have an increased width of the depletion region, which facilitates the collection of carriers. The overall recombination of the device, including the absorber bulk and the interface, is inhibited. Accordingly, the performance of CZTSSe solar cells is significantly improved. This study breaks the bottleneck in the development of kesterite solar cells.

## 2. Results and Discussion

### 2.1. N-Type Surface Design and Construction

The as-grown  $\text{Ag}_2\text{ZnSnS}_4$  (AZTS) precursor film is crystallized in the tetragonal structure with poor crystallization and has n-type behavior according to Hall effect test results (Figure S1 and Table S1, Supporting Information). Therefore, we designed a new structure (Figure 1a) to prepare the absorber layer, that is,  $\text{Al}_2\text{O}_3$  was deposited on the as-grown  $\text{Cu}_2\text{ZnSnS}_4$  (CZTS) precursor film using 3-cycles of atomic layer deposition (ALD, NCE-200R, NanoFrontier), and then the AZTS precursor ink ( $\approx 50$  nm thick, as calculated from the spin-coating thickness shown in S1(d), Supporting Information) was spin-coated onto the surface of the CZTS/ALD- $\text{Al}_2\text{O}_3$  heterojunction film. All the precursor films, including pure CZTS precursor film without ALD- $\text{Al}_2\text{O}_3$  and AZTS and those with ALD- $\text{Al}_2\text{O}_3$  and AZTS, underwent a high-temperature selenization process at 570 °C to prepare the absorber layer. The CZTSSe absorber layer obtained by selenizing pure CZTS precursor film without ALD- $\text{Al}_2\text{O}_3$  and AZTS and the one with ALD- $\text{Al}_2\text{O}_3$  and AZTS are referred to as sample Kes and sample Kes- $\text{Al}_2\text{O}_3$ -AZTS, respectively, and the corresponding solar cells are named cell-Kes and cell-Kes- $\text{Al}_2\text{O}_3$ -AZTS, respectively.

Figure 1b shows the X-ray diffraction (XRD) patterns of samples Kes and Kes- $\text{Al}_2\text{O}_3$ -AZTS, wherein only diffraction peaks belonging to CZTSSe are observed for both types of films.<sup>[22–24]</sup> and the full-width at half maximum of sample Kes- $\text{Al}_2\text{O}_3$ -AZTS is smaller, indicating that its crystallization is better. The magnified (112) peak of sample Kes- $\text{Al}_2\text{O}_3$ -AZTS moves to a smaller angle compared with that of sample Kes, which should be ascribed to Ag incorporation into the absorber film because of the larger radius of Ag compared with that of Cu.<sup>[16,25]</sup> The Raman spectra excited at a 532 nm excitation wavelength shown in Figure 1c confirm that the prepared films are composed of the phase with the kesterite structure.<sup>[26,27]</sup> It is also observed in Figure 1d that the Raman peak of sample Kes- $\text{Al}_2\text{O}_3$ -AZTS is red-shifted compared with that of sample Kes because of the existence of Ag on the surface of the absorber film,<sup>[16]</sup> which is consistent with the XRD results. The characteristic peak of the B-mode ( $\approx 172$   $\text{cm}^{-1}$ ) decreases for sample Kes- $\text{Al}_2\text{O}_3$ -AZTS, which indicates that the density of  $[\text{V}_{\text{Cu}} +$

$\text{Zn}_{\text{Cu}}]$  clusters increases and the Cu content on the film surface decreases.<sup>[28,29]</sup> Additionally, the E-mode ( $\approx 234$   $\text{cm}^{-1}$ ) intensity decreases for sample Kes- $\text{Al}_2\text{O}_3$ -AZTS, indicating that the density of detrimental  $[\text{2Cu}_{\text{Zn}} + \text{Sn}_{\text{Zn}}]$  is significantly reduced.<sup>[28,30,31]</sup> In other word, the optoelectronic properties of the surface of sample Kes- $\text{Al}_2\text{O}_3$ -AZTS are effectively modified compared to that of the sample Kes.

Grazing-incidence X-ray diffraction (GIXRD) was conducted on sample Kes- $\text{Al}_2\text{O}_3$ -AZTS to observe the distribution of Ag, as shown in Figure 1e. The characteristic peaks of CZTSSe are observed, and the (112) peaks shift to a larger angle as the grazing incidence angle gradually increases to 1° (Figure 1f), indicating that Ag is incorporated into the crystal lattice and distributed more at the surface. When the grazing incidence angle is further increased, the (112) peaks do not move apparently. The X-ray penetration depth in the absorber film can be calculated according to the following equation:<sup>[32,33]</sup>

$$z = \frac{1}{\mu} \left( \frac{1}{\sin a_i} + \frac{1}{\sin(2\theta - a_i)} \right)^{-1} \quad (1)$$

where  $z$  is the penetration depth,  $a_i$  is the incidence angle,  $2\theta$  is the Bragg angle, and  $\mu$  is the attenuation coefficient. Thus, the calculated thickness of the portion of the absorber film incorporating Ag should be  $\approx 150$ –300 nm.

Atomic force microscope (AFM) and Kelvin probe force microscope (KPFM) measurements are performed to observe the spatial topography and surface contact potential difference (CPD) images of sample Kes and sample Kes- $\text{Al}_2\text{O}_3$ -AZTS, as shown in Figure 2. From the AFM topography images, the particles of sample Kes- $\text{Al}_2\text{O}_3$ -AZTS are significantly larger than those of sample Kes, which is consistent with the XRD results shown in Figure 1b because Ag acts as a flux to effectively promote the growth of large crystals.<sup>[5,8,19]</sup> CPD images can provide nano-level surface information related to surface defects and stoichiometry.<sup>[34,35]</sup> Figure 2b,e show the surface electric potentials of sample Kes and sample Kes- $\text{Al}_2\text{O}_3$ -AZTS, respectively. The CPD of the grain boundaries (GBs) of these two samples is higher than that inside the crystal grains, and causes downward band bending at the GBs, which leads to reduced charge carrier recombination and enhanced carrier separation.<sup>[36,37]</sup> The average CPD of sample Kes is  $-230$  mV (Figure 2c), which is similar to that of p-type CZTSSe films.<sup>[11,35,38]</sup> However, it is very surprising that the average CPD of sample Kes- $\text{Al}_2\text{O}_3$ -AZTS is  $+111$  mV (Figure 2f). These results indicate the average Fermi energy level ( $E_F$ ) at the surface of sample Kes- $\text{Al}_2\text{O}_3$ -AZTS (in the range of 100  $\approx$  400 nm in S2, Supporting Information) is increased by 0.34 eV ( $111 + 230 = 340$  meV).<sup>[38,39]</sup>

To clarify the reason why the CPD of sample Kes- $\text{Al}_2\text{O}_3$ -AZTS is positive, we characterized the depth-dependent X-ray photoelectron spectroscopy (XPS) of sample Kes- $\text{Al}_2\text{O}_3$ -AZTS, and the results are shown in S3, Supporting Information. (The sample was sputtered from 0 to 850 s). The binding energies are calibrated using the core level of C 1s (284.8 eV).<sup>[40]</sup> The Cu 2p peaks at 932.2 and 952.0 eV show a binding energy difference of 19.8 eV, which is indicative of Cu(I) (Figure 3a). The Ag 3d spin orbitals ( $3d_{5/2}$  at 368.1 eV and  $3d_{3/2}$  at 374.1 eV) with doublet separation of 6.0 eV can be assigned to Ag(I),<sup>[16,41]</sup> as shown in Figure 3b. With the increase of detection time, the intensity of

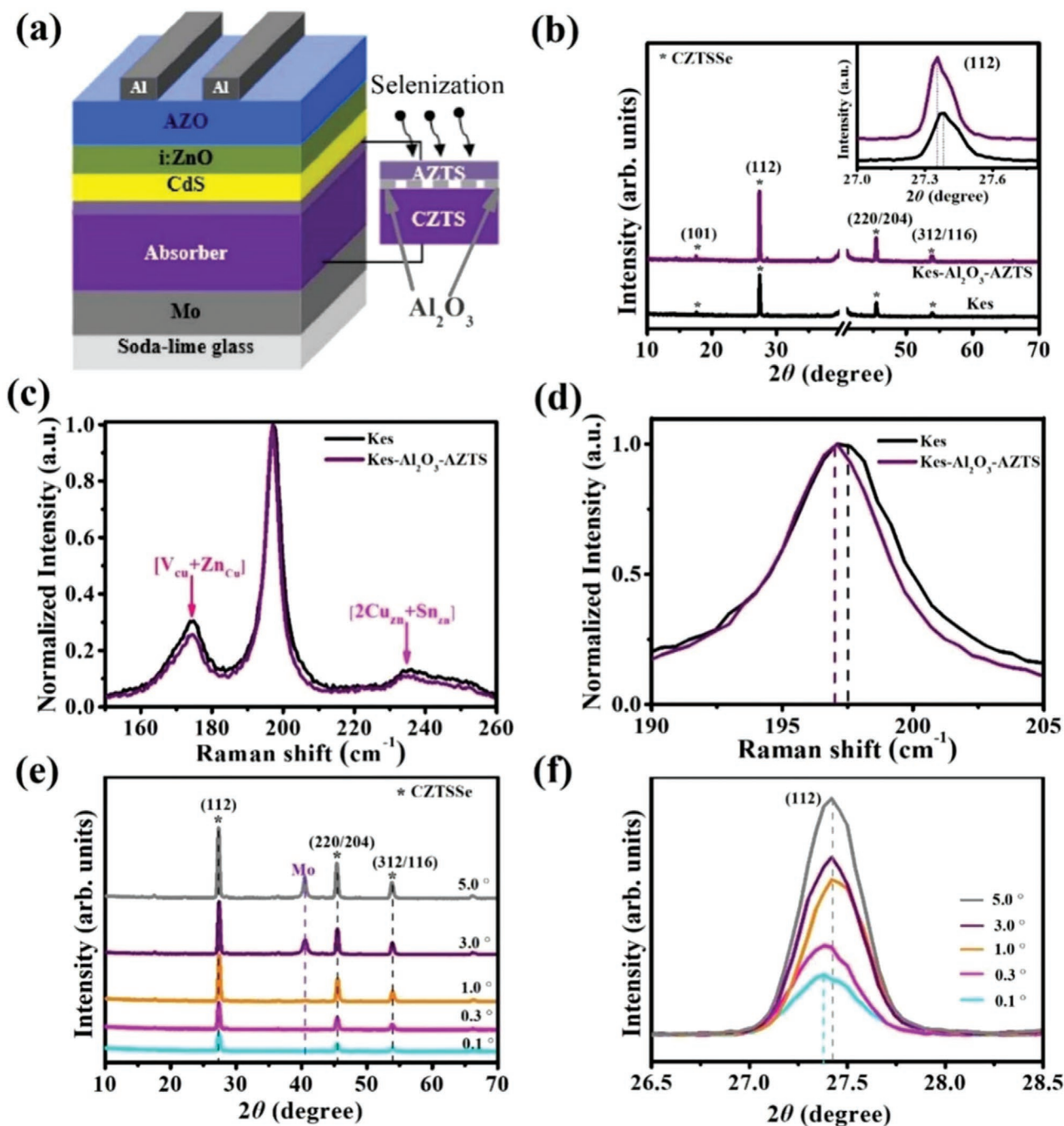


**Figure 1.** a) The device structure of cell-Kes- $\text{Al}_2\text{O}_3$ -AZTS.  $\text{Al}_2\text{O}_3$  is inserted between the precursor CZTS and AZTS by atomic layer deposition, and they are selenized at high temperature to obtain the final absorber layer. b) XRD patterns of sample Kes and sample Kes- $\text{Al}_2\text{O}_3$ -AZTS, and magnified patterns of the (112) peaks (inset). c) The normalized Raman spectra of sample Kes and sample Kes- $\text{Al}_2\text{O}_3$ -AZTS, and d) the magnified A-mode. GIXRD patterns of sample Kes- $\text{Al}_2\text{O}_3$ -AZTS at different grazing-incidence angles e) and magnified patterns of the (112) peaks f).

the Cu signal peak is gradually increasing, and the intensity of the Ag signal peak is gradually decreasing, implying that the Cu content from the surface into the bulk gradually increases and the Ag content gradually decreases.<sup>[41]</sup> The ratio of  $\text{Ag}/(\text{Ag} + \text{Cu})$  calculated from the XPS results gradually decreases from 50.64% to 46.86% with the increase of the detection depth of the film (see detailed calculation information of Ag 3d and Cu 2p by semi-quantitative analysis shown in Table S3, Supporting

Information). The EDS line-scan from the transmission electron microscope (TEM) image for sample Kes- $\text{Al}_2\text{O}_3$ -AZTS shown in S4, Supporting Information also indicates that the intensity of the Ag signal is higher than the Cu signal at the surface depth region of  $\approx 30$  nm. The above results are consistent with the GIXRD and Raman results shown in Figure 1. It has been reported that the Ag-doped CZTSSe is n-type when the Ag content is at or exceeds 50%.<sup>[15]</sup> Thus, in this study, we



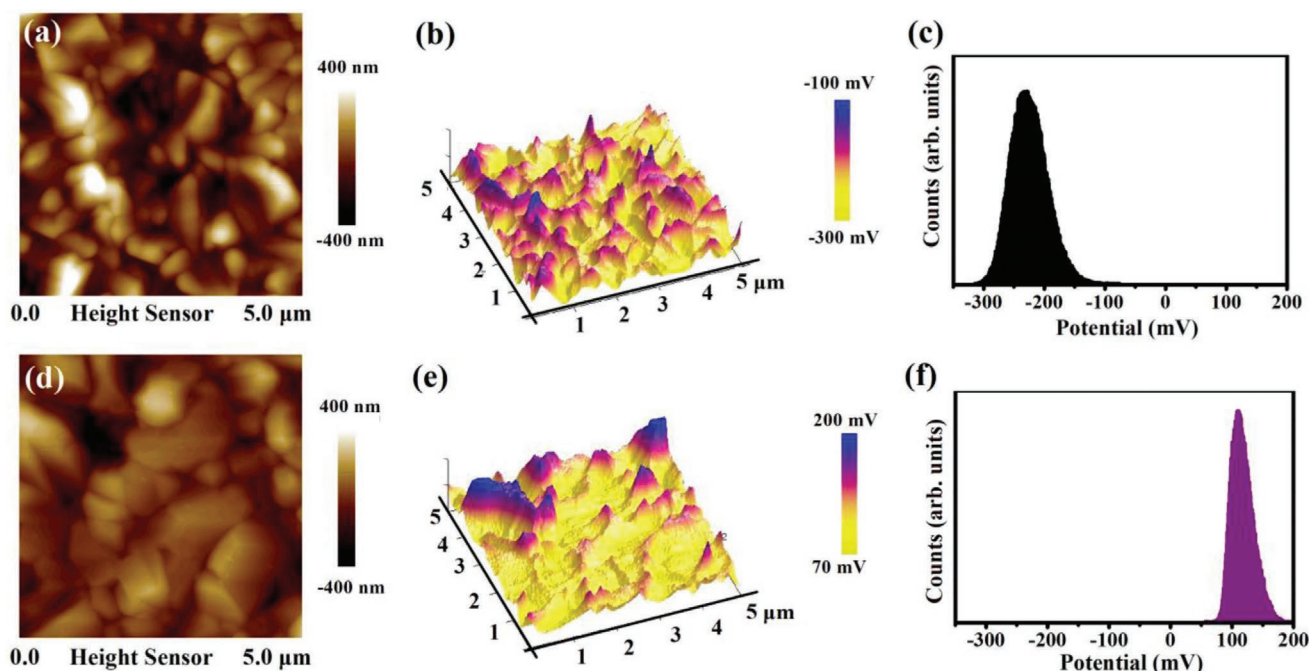


**Figure 2.** AFM topography images a,d), KPFM potential maps b,e), and surface contact potential difference distributions c,f). a–c) for sample Kes; d–f) for sample Kes- $\text{Al}_2\text{O}_3$ -AZTS.

can deduce that an n-type surface in sample Kes- $\text{Al}_2\text{O}_3$ -AZTS should be realized. S4(b), Supporting Information also confirms that the Al signal is very low. In addition, the S signal in the absorber is close to 0, suggesting our film is Se-rich, which also supports the previous research results of our group.<sup>[9,11,42]</sup>

To further verify that Ag is doped into the surface of the absorber layer and thus results in an n-type surface, high-resolution TEM (HRTEM) and selected-area electron diffraction (SAED) are performed. To determine the lattice difference, the top and the interior of the absorber layer are selected for characterization (the selected areas are shown in S4, Supporting Information). The HRTEM lattice fringes shown in Figure 3c indicate that the interplanar distance (d-space) of the (112) planes is 0.335 nm on the top of the sample Kes- $\text{Al}_2\text{O}_3$ -AZTS, while the distance between adjacent (112) planes of  $\text{Ag}_2\text{ZnSnSe}_4$  is 0.341 nm.<sup>[43]</sup> The HRTEM lattice fringes shown in Figure 3d indicate that the interplanar distance of (112) planes is 0.326 nm in the interior area of the sample Kes- $\text{Al}_2\text{O}_3$ -AZTS, and this value is close to 0.328 nm (JCPDS #52-868) of the d-space of (112) planes of kesterite-structure  $\text{Cu}_2\text{ZnSnSe}_4$ .

The corresponding SAED patterns and the crystal plane clusters obtained by simulation are shown in Figure 3(e) and (f). The angle between the (002) crystal plane and the (12) crystal plane in the SAED pattern (Figure 3(e)) measured on the top of the absorber layer is  $\approx 53.9^\circ$ , which is close to the theoretical angle of  $56.3^\circ$  of  $\text{Ag}_2\text{ZnSnSe}_4$ . The measured angle between the (112) and (01) crystal planes in the electron diffraction pattern (Figure 3f) inside the absorber layer is  $75^\circ$ , which is consistent with the theoretical angle of  $\text{Cu}_2\text{ZnSnSe}_4$ . In summary, the above results prove that the top of sample Kes- $\text{Al}_2\text{O}_3$ -AZTS has the Ag-rich kesterite structure, while the internal structure

of the sample is closer to the CZTSe phase, and the Se content in the two substances is much higher than that of S.

Figure 4 shows the XPS valence band spectra of sample Kes- $\text{Al}_2\text{O}_3$ -AZTS with different detection depths, from which the valence band maximum (VBM) positions can be estimated. As the etching time increases, the VBM position gradually decreases from 0.63 eV (0 s etching) below the  $E_F$  to 0.12 eV (850 s etching). These results show that the VBM of the absorber layer gradually moves away from its Fermi level position and the difference is  $0.63 - 0.12 = 0.51$  eV from the bulk to the top surface.

To further investigate the effective process for realizing an n-type surface, two other experiments with distinct constructions were carried out. As shown in S5, Supporting Information, the first additional experiment involved the same thick AZTS layer spin-coated directly onto the surface of the as-grown absorber followed by the same selenization process (S5a, Supporting Information). In addition to the large particles seen in the image measured by scanning electron microscope (SEM) shown in S5b, Supporting Information, there are also many nano-scale grains belonging to poorly crystallized AZTS covering the large particles. Unfortunately, the sample is apt to dissolve in water, thus causing the film to fall off the Mo electrode when growing CdS by the chemical bath deposition method because of residual solvent, even with the pre-annealing temperature increased to  $450^\circ\text{C}$ . The second additional experiment is that the same AZTS precursor film is directly spin-coated onto the original CZTS precursor, and then they are subjected to the same selenization as sample Kes- $\text{Al}_2\text{O}_3$ -AZTS to prepare the completed absorber layer, referred to as sample Kes-AZTS, and the corresponding solar cell is named cell-Kes-AZTS (S5c Supporting Information). According to the kinetic study of Ag,

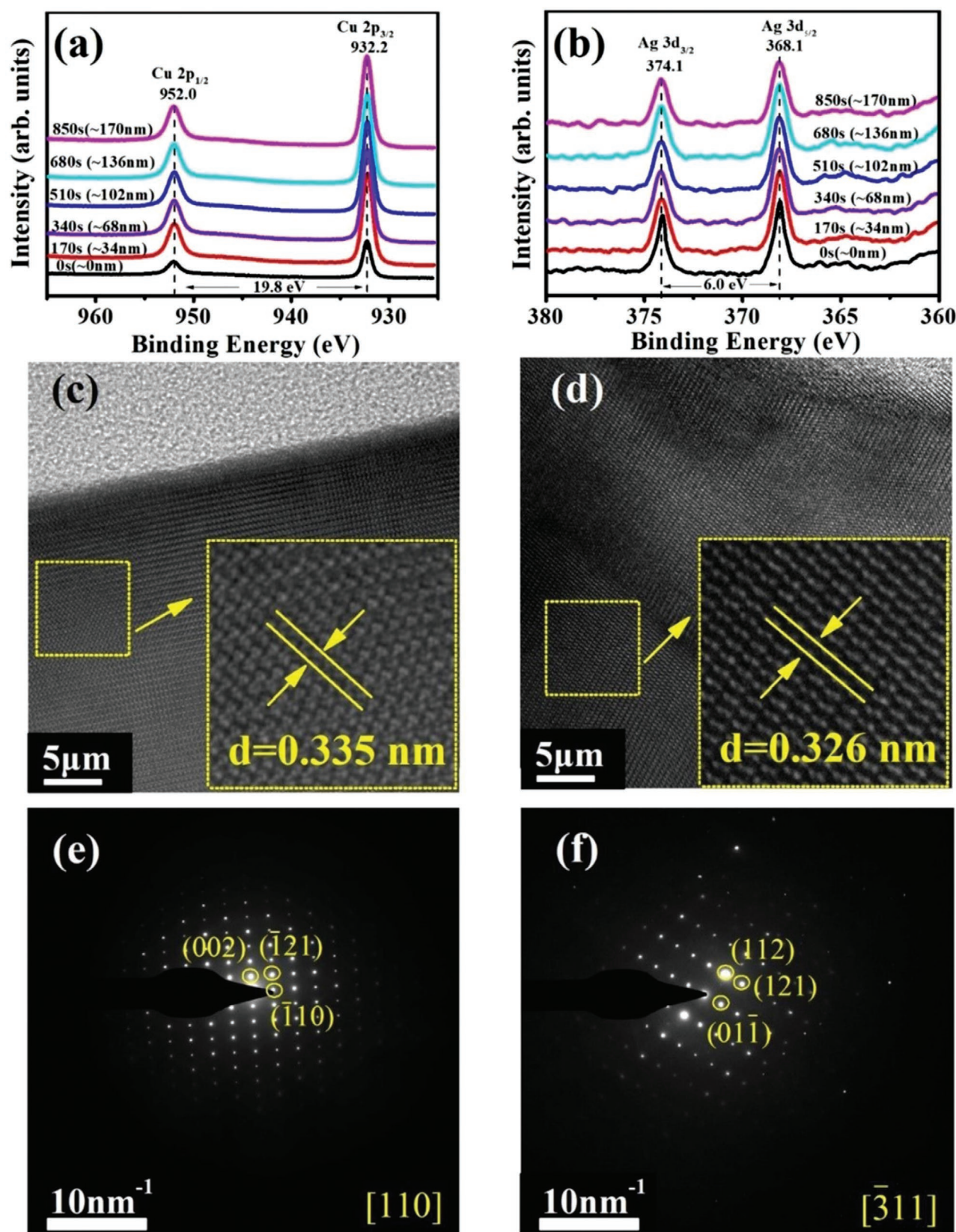


**Figure 3.** XPS spectra of a) Cu 2p and b) Ag 3d core levels of sample Kes-Al<sub>2</sub>O<sub>3</sub>-AZTS. c,d) High resolution TEM images and e,f) the corresponding selected area electron diffraction patterns. c,e) for the top and d,f) for the interior of sample Kes-Al<sub>2</sub>O<sub>3</sub>-AZTS.



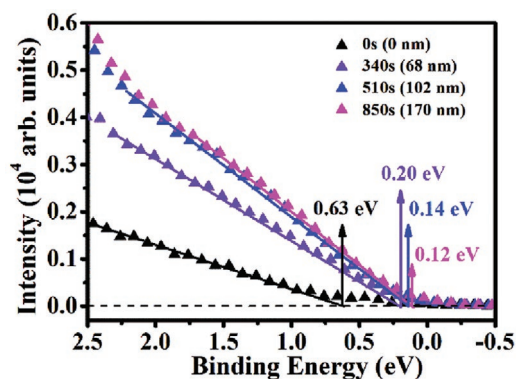


**Figure 4.** XPS valence band data for sample Kes-Al<sub>2</sub>O<sub>3</sub>-AZTS with etching for 0 s, 340 s, 510 s, and 850 s.

the treatment temperature is proportional to the diffusion rate of the element.<sup>[5,8,15]</sup> In order to control the diffusion behavior of Ag in the absorber layer, the selenization temperature is decreased accordingly, and the corresponding XRD patterns are shown in S5d, Supporting Information. Secondary phases are detected in the samples (i.e., SnSe<sub>2</sub>, AgSnSe<sub>2</sub>) when the temperature is too low. Only three main diffraction peaks belonging to CZTSSe are observed,<sup>[24]</sup> and no other secondary phases are found when the selenization temperature reaches 530 °C. However, with the increase in the grazing incidence angle, there is no shift of the (112) peak of the film selenized at 530 °C in the GIXRD result shown in S5e, Supporting Information. The photovoltaic performance of the best solar cell (S5f Supporting Information) fabricated by this approach is almost unchanged compared with cell-Kes (in which the absorber layer of the device is obtained only by selenization of the CZTS precursor film).

These results indicate that: (a) The direct growth of n-type AZTS on the as-grown p-type CZTSSe layer cannot be used to successfully fabricate solar devices. (b) When directly growing n-type AZTS on the CZTS precursor film, even if the post-selenization temperature is decreased, the Ag distribution cannot be effectively controlled. (c) A suitable ALD-Al<sub>2</sub>O<sub>3</sub> layer is necessary for forming an n-type surface, and then the Ag distribution behavior in sample Kes-Al<sub>2</sub>O<sub>3</sub>-AZTS is easily controlled. This strategy breaks the belief that it is difficult to form an n-type layer on the surface of CZTSSe like in CIGSSe.

## 2.2. Device Performance

Next, the performance of devices utilizing the n-type surface layer formation strategy is studied. According to the resulting performance statistics (Figure 5a), the average cell efficiency is 11.8% for cell-Kes-Al<sub>2</sub>O<sub>3</sub>-AZTS devices, and the average  $V_{OC}$  has been significantly increased from 430 meV (cell-Kes) to 499 meV (cell-Kes-Al<sub>2</sub>O<sub>3</sub>-AZTS), approximately a 69 meV improvement. Furthermore, the average current density ( $J_{SC}$ ) increases 3.5 mA cm<sup>-2</sup> from 31.3 (Cell-Kes) to 34.8 mA cm<sup>-2</sup>. At the same time, the average fill factor ( $FF$ ) displays the same growth trend. The champion power conversion efficiency of 12.55% with  $J_{SC}$ ,  $V_{OC}$ , and  $FF$  of 35.0 mA cm<sup>-2</sup>, 526 mV, and 68.2% is achieved for cell-Kes-Al<sub>2</sub>O<sub>3</sub>-AZTS, as shown in Figure 5b.

In order to study whether the main reason for the efficiency improvement of the cell-Kes-Al<sub>2</sub>O<sub>3</sub>-AZTS devices is the n-type surface of the absorber layer caused by Ag doping, we conduct the following comparative tests: cell-Kes-Al<sub>2</sub>O<sub>3</sub> (in which the absorber layer is obtained by only growing 3-cycles of Al<sub>2</sub>O<sub>3</sub> on the CZTS film followed by selenization) and cell-Kes-Al<sub>2</sub>O<sub>3</sub>-Kes (in which the absorber layer of the device is obtained by growing 3-cycles of Al<sub>2</sub>O<sub>3</sub> onto CZTS film then spin-coating the CZTS precursor ink ( $\approx 50$  nm thick) onto the surface followed by selenization). The statistical results from 36 devices of each device type are shown in S6, Supporting Information. The values of all device parameters of cell-Kes-Al<sub>2</sub>O<sub>3</sub> are higher than those of cell-Kes, and the average efficiency is increased from 8.2% (cell-Kes) to 9.8% (cell-Kes-Al<sub>2</sub>O<sub>3</sub>), mainly due to the improvement of  $V_{OC}$  and  $FF$ . To investigate the effect of 3-cycles of ALD-Al<sub>2</sub>O<sub>3</sub> on the surface of the absorber layer, we performed X-ray photoelectron spectroscopy measurements on samples Kes and Kes-Al<sub>2</sub>O<sub>3</sub>, and the results are shown in S7, Supporting Information. It is found that there is almost no shift in the binding energy for all elements in these two samples. The binding energy of Al 2p is close to the Cu 3p peak, and thus the XPS spectra of Cu 3p and Al 2p are plotted together in S7(f), Supporting Information. Sample Kes-Al<sub>2</sub>O<sub>3</sub> is fitted with two peaks (red and blue lines) corresponding to the binding energy of Al 2p, indicating the device performance enhancement for cell-Kes-Al<sub>2</sub>O<sub>3</sub> is partly attributed to passivation by the ALD-Al<sub>2</sub>O<sub>3</sub> layer.<sup>[44,45]</sup> The parameters of the cell-Kes-Al<sub>2</sub>O<sub>3</sub>-AZTS devices are further improved from those of cell-Kes-Al<sub>2</sub>O<sub>3</sub> devices. In addition, if the thin CZTS layer is spin-coated on the upper layer of sample Kes-al, the corresponding solar cell performance (cell-Kes-Al<sub>2</sub>O<sub>3</sub>-Kes) is slightly worse than that of cell-Kes-Al<sub>2</sub>O<sub>3</sub>, which is mainly reflected in  $V_{OC}$  and  $FF$ . These results imply the unique positive effect of Ag incorporation through the Ag doping strategy proposed in this work.

The external quantum efficiency (EQE) response (Figure 5c) of cell-Kes-Al<sub>2</sub>O<sub>3</sub>-AZTS reflects greater carrier collection efficiency than cell-Kes from  $\approx 400$  to  $\approx 1100$  nm, suggesting the quality of the front interface and bulk have been improved with a positive effect on carrier collection. The average band gaps of the absorber films estimated from the EQE data (Figure 5d) are 1.063 eV for device cell-Kes and 1.072 eV for cell-Kes-Al<sub>2</sub>O<sub>3</sub>-AZTS, and this may be a reason for the increase in  $V_{OC}$ . The band gap of 1.072 eV is lower than that of 1.086 eV for cell-Kes-AZTS (S8, Supporting Information), but the  $V_{OC}$  is 90 meV higher. The  $V_{OC}$  deficits are calculated with respect to the maximum theoretical value represented by the Shockley-Queisser limit.<sup>[46]</sup> In that regard, the different band gaps of the materials are considered, hence making the comparison realistic. Then, the  $V_{OC}$  deficit is estimated as follows:<sup>[47,48]</sup>

$$V_{OC,def} = V_{OC}^{SQ} - V_{OC}^{exp} \quad (2)$$

$$V_{OC}^{SQ} = 0.932 \times E_g - 0.167 \quad (3)$$

where  $V_{OC}^{SQ}$  is the maximum thermodynamic  $V_{OC}$  achievable for a given absorber band gap, and  $V_{OC}^{exp}$  is the  $V_{OC}$  obtained from the  $J$ - $V$  analysis under AM1.5G conditions. Most commonly, the band gap value  $E_g$  used for estimating the  $V_{OC}^{SQ}$  is extracted from the external quantum efficiency. Compared with other CZTSSe-based

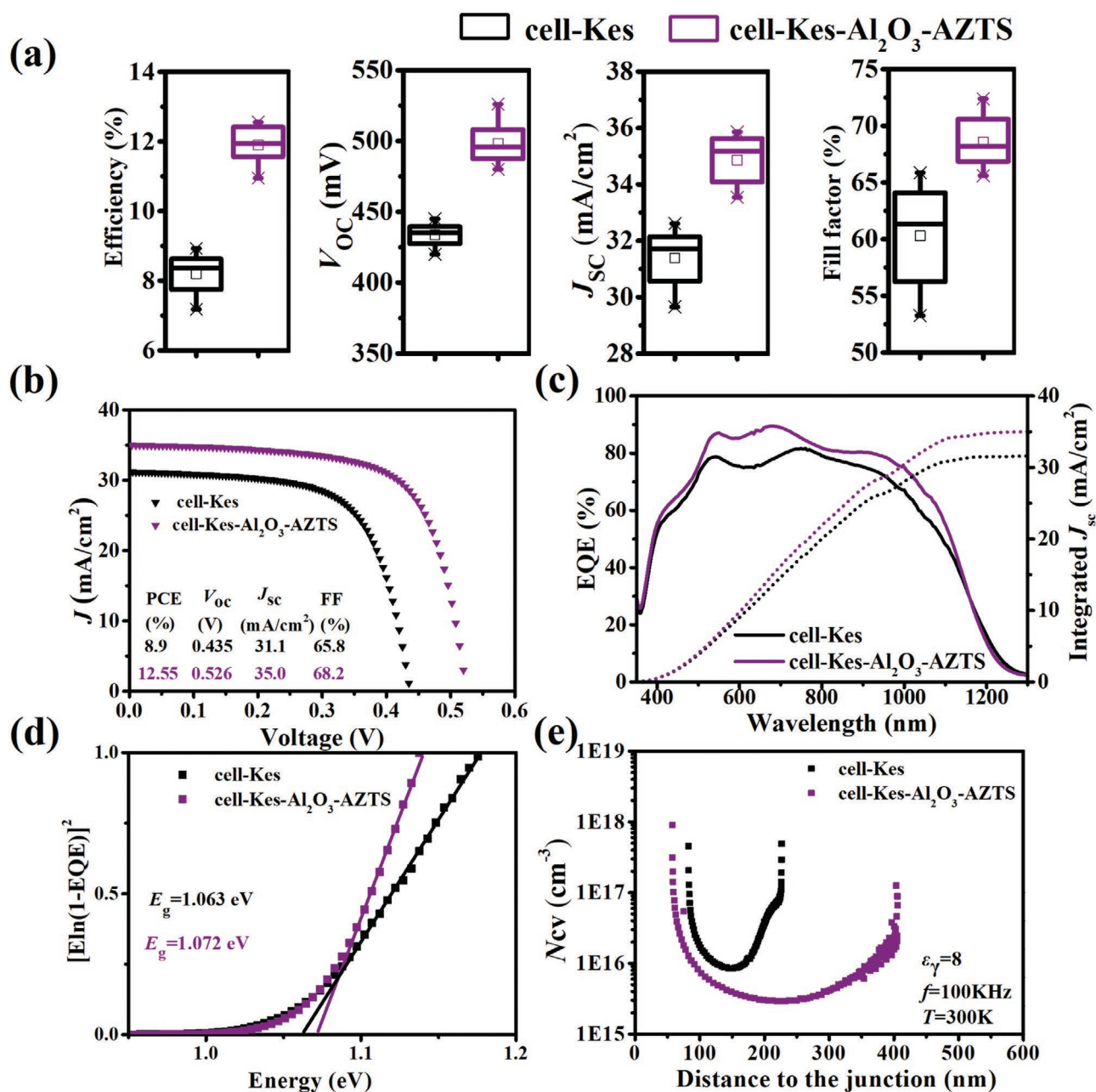


**Figure 5.** a) The statistical photovoltaic performances of 36 devices of each device type (cell-Kes and cell-Kes-Al<sub>2</sub>O<sub>3</sub>-AZTS). b)  $J-V$  curves of the champion cell-Kes and cell-Kes-Al<sub>2</sub>O<sub>3</sub>-AZTS devices. c) EQE spectra and the integrated  $J_{SC}$  of cell-Kes and cell-Kes-Al<sub>2</sub>O<sub>3</sub>-AZTS. d) Band gap estimations by fitting the expected linear region of the EQE data. e) C-V curves of the best cells.

solar cells (Table S4, Supporting Information), the 12.55% efficiency of this work is very close to the record efficiency of 12.6%,<sup>[1]</sup> and it has a lower  $V_{OC}$  deficit of 0.306 V (63.2% Shockley-Queisser limit, cell-Kes-Al<sub>2</sub>O<sub>3</sub>-AZTS), demonstrating the advantage of this new strategy with Ag for achieving high-quality kesterite solar cells. The ideality factor ( $A$ ) of the best devices is reduced from  $\approx 1.95$  of cell-Kes to  $\approx 1.52$  of cell-Kes-Al<sub>2</sub>O<sub>3</sub>-AZTS shown in S9, Supporting Information suggesting that recombination within the space-charge region has been reduced,<sup>[49]</sup> and a reduced series resistance ( $R_s$ ) is related to the increased FF. The reduced  $V_{OC,def}$  for cell-Kes-Al<sub>2</sub>O<sub>3</sub>-AZTS

should be attributed to the reduced nonradiative recombination as the reverse saturation current density  $J_0$  (single-diode model) is decreased by two orders of magnitude. Figure 5(e) shows calculated results from the capacitance-voltage (C-V) data of cell-Kes and cell-Kes-Al<sub>2</sub>O<sub>3</sub>-AZTS shown in S10, Supporting Information. The depletion region increases from 191 (cell-Kes) to 275 nm (cell-Kes-Al<sub>2</sub>O<sub>3</sub>-AZTS), which is conducive to carrier collection.

To further understand the reasons for efficiency improvement, especially the  $V_{OC,def}$  and FF, the temperature-dependent admittance spectra (AS) measurements are performed, as

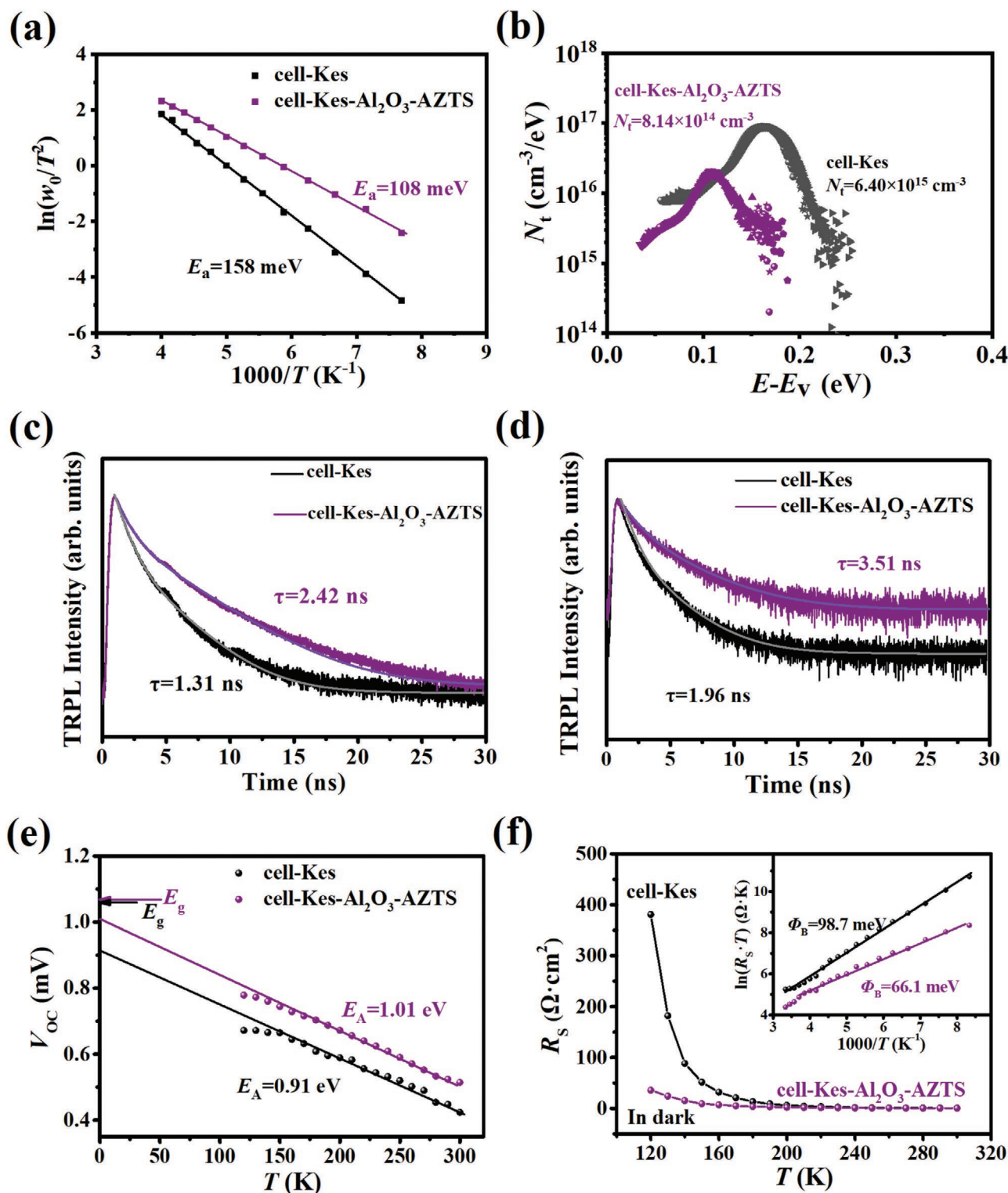


**Figure 6.** a) Arrhenius plots derived from the admittance results and b) the density of defect states estimated from the admittance results for cell-Kes and cell-Kes-Al<sub>2</sub>O<sub>3</sub>-AZTS, respectively. Normalized TRPL decay obtained at excitation wavelengths of c) 532 nm and d) 808 nm for the devices cell-Kes and cell-Kes-Al<sub>2</sub>O<sub>3</sub>-AZTS. e) The temperature dependent open circuit voltage of these two solar cells and their linear extrapolation to  $T = 0$  K. f) Temperature dependent series resistance extracted from the dark current-voltage data. Inset: barrier height extracted from  $\ln(R_s T)$  versus  $1000/T$ .

shown in S11, Supporting Information. The relevant defect level ( $E_a$ ) and the defect density ( $N_t$ ) calculations are provided (see the details of admittance data analysis in Supplementary Note 2

of Supporting Information).<sup>[31,50]</sup> As depicted in Figure 6a,b,  $E_a$  and  $N_t$  for cell-Kes are 158 meV and  $6.40 \times 10^{15}$  cm<sup>-3</sup>, and those for cell-Kes-Al<sub>2</sub>O<sub>3</sub>-AZTS are 108 meV and  $8.14 \times 10^{14}$  cm<sup>-3</sup>,



respectively. According to the first principle calculation and previous experimental observations, the defect level of  $\text{Cu}_{\text{Zn}}$  is around  $110 \approx 217$  meV.<sup>[30,51,52]</sup> Therefore, both kinds of defects measured in cell-Kes and cell-Kes- $\text{Al}_2\text{O}_3$ -AZTS should be assigned as  $\text{Cu}_{\text{Zn}}$  anti-sites. The shallower activation energy and lower concentration of  $\text{Cu}_{\text{Zn}}$  in cell-Kes- $\text{Al}_2\text{O}_3$ -AZTS could be attributed to the incorporation of Ag in the kesterite lattice, as Ag alloying is known to reduce the p-type doping in kesterite materials.<sup>[15]</sup> The lower density of acceptor-like defects and associated lower carrier density in cell-Kes- $\text{Al}_2\text{O}_3$ -AZTS has resulted in a larger depletion region as shown in  $C$ - $V$  measurements, which facilitates the carrier collection efficiency under the condition of low minority carrier lifetime as will be discussed below.<sup>[23]</sup> The lower carrier density may reduce the quasi-Fermi level splitting in the quasi-neutral region, thus limiting the increase of  $V_{\text{OC}}$ .<sup>[27]</sup> On the other hand, the lower acceptor-like defects and shallower acceptor defects could effectively reduce the interface non-radiative recombination by means of reducing the  $N_{\text{A}}$ , increasing the hole lifetime at interface ( $\tau_{\text{p}}$ ), and increasing the band bending ( $qV_{\text{b}}$ ) according to the heterojunction interface recombination model established by Li et al.<sup>[53]</sup> In a word, the reduced density and activation energy of acceptor-like defects induced by incorporation of Ag on top of CZTSSe absorber may significantly promote the carrier collection efficiency and may also greatly contribute to the increase of  $V_{\text{OC}}$  by reducing the non-radiative interface recombination.

Figure 6c,d shows the time-resolved photoluminescence (TRPL) decay data of the devices cell-Kes and cell-Kes- $\text{Al}_2\text{O}_3$ -AZTS measured using 532 and 808 nm lasers, respectively. The measurements using 532 nm laser are sensitive to the recombination processes occurring at the p-n junction interface (i.e., mostly at the surface region of absorber layer), whereas the measurements using 808 nm laser probes carrier recombination more uniformly distributed throughout the bulk.<sup>[49]</sup> The decay times of device cell-Kes- $\text{Al}_2\text{O}_3$ -AZTS are larger than those of device cell-Kes measured using both lasers (See the specific process of fitting and the obtained lifetime  $\tau_1$  and  $\tau_2$  in Table S5, Supporting Information). The increase of PL decay time measured using 532 nm laser may further contribute to the reduce of interface recombination, whilst the increase of PL decay time measured using 808 nm laser may further contribute to the improvement on carrier collection efficiency, but with slight contribution to the increase of  $V_{\text{OC}}$ .

Figure 6e shows the temperature-dependent open-circuit voltage ( $V_{\text{OC}}-T$ ) of the above two devices for further investigation of interface recombination.  $E_{\text{g}}$  indicates the optical bandgap of the absorber layer derived from EQE data and the recombination activation energy  $E_{\text{A}}$  is the y-axis extrapolation of linear fits to  $T = 0$  K. The values of  $E_{\text{A}}$  of the two devices are smaller than that of the  $E_{\text{g}}$ , indicating that both devices have additional interface recombination, which may be at the front interface or the back interface.<sup>[9,29,49]</sup> The  $E_{\text{A}}$  of the cell-Kes- $\text{Al}_2\text{O}_3$ -AZTS is 0.1eV larger than that of the cell-Kes, which is in good accordance with the 91 mV  $V_{\text{OC}}$  increase. This further consolidates that most of the  $V_{\text{OC}}$  improvement may come from the reduced front interface recombination. The temperature-dependent photovoltaic performance of devices cell-Kes and cell-Kes- $\text{Al}_2\text{O}_3$ -AZTS is shown in S12,13, Supporting Information. The efficiency and  $J_{\text{SC}}$  of both devices collapse quickly at

low temperature ( $\approx 160$  K), as well as the collapse of FF, which should be attributed to the dramatically increased series resistance (Figure 6f). Similar behavior has been observed in other CZTSSe solar cells.<sup>[54,55]</sup> The obtained blocking barrier heights ( $\Phi_{\text{B}}$ ) for cell-Kes and cell-Kes- $\text{Al}_2\text{O}_3$ -AZTS are 98.7 meV and 66.1 meV, respectively (see the detailed calculations in Supplementary Note 3). Therefore, besides the recombination at the interface and space charge region, the FF of these cells is also limited by the back contact blocking barrier.<sup>[9,24,56]</sup>

### 3. Conclusion

In this study, we design and construct Ag-doped CZTSSe thin film to enable a power conversion efficiency of 12.55% with a  $V_{\text{OC,def}}$  of only 0.306 V without an anti-reflection layer. Encouragingly, the p-type absorber surface n-type layer and the Ag gradient band gap are both successfully prepared. The inversion layer increases the difference of the quasi-Fermi levels of the absorber surface, which is beneficial to increase the open circuit voltage. The surface valence band gradient regulates the carrier transport and the increase in the width of the depletion region also helps the collection of carriers. This novel Ag doping strategy reduces the recombination at the interface and absorber bulk, which will promote the manufacture and performance optimization of high-performance CZTSSe solar cells.

### 4. Experimental Section

**Preparation of Precursor Film:**  $(\text{CH}_3\text{COO})_2\text{Cu} \cdot \text{H}_2\text{O}$  (Aladdin, 99.95%, 2.296 g) or  $\text{AgNO}_3$  (InnoChem, 99.99%, 1.954 g),  $\text{SnCl}_2 \cdot 2\text{H}_2\text{O}$  (Aladdin, 99.99%, 1.805 g) or  $\text{SnCl}_4$  (Aladdin, 99%, 2.08 g),  $\text{ZnCl}_2$  (Aladdin, 99.95%, 1.090 g), and  $\text{H}_2\text{NCSNH}_2$  (InnoChem, 99.0%, 2.721 g) were sequentially added to Dimethyl sulfoxide (Aladdin, 99.9%, 10 mL) and magnetically stirred to form the clear precursor solution of CZTS and AZTS in an argon-filled glovebox ( $\text{H}_2\text{O}$  and  $\text{O}_2$  levels maintained  $\leq 1$  ppm). The specific steps and details of the CZTS precursor solution can be found in our previous work.<sup>[22,42]</sup> The preparation steps of AZTS precursor solution were similar to those of CZTS, and digital photographs of these steps are shown in S1a, Supporting Information. The precursor solutions were coated onto Mo-deposited glass substrates or glass followed by annealing on a hot plate in the glovebox and these steps were repeated several times to obtain the desired precursor films.

**Preparation of Absorber Layer and Solar Cell:** The precursor films were put into a graphite box with Se powder ( $\approx 800$  mg) and placed in a rapidly heating furnace tube (OTF-1200X) for selenization. Then the tube was evacuated and refilled with nitrogen to a pressure of  $\approx 440$  Torr. Finally, the selenization was performed at  $570^\circ\text{C}$  for 20 min followed by natural cooling.

Solar cell devices were fabricated with the configuration SLG/Mo/absorber layer/ $\text{CdS}/\text{i-ZnO}/\text{Al-ZnO}/\text{Al}$ . The solar cell area of  $0.18\text{ cm}^2$  was defined by mechanical scribing. No etching or anti-reflection layers were used in this work.

**Characterization:** A Bruker D8 ADVANCE X-ray diffractometer with  $\text{Cu K}_\alpha$  radiation ( $\lambda = 0.1542\text{ nm}$ ) and a LabRAM-HR Evolution Raman spectrometer (Horiba Jobin Yvon) equipped with a 532 nm laser with the power excitation density  $\approx 60\text{ mW cm}^{-2}$  were used to characterize the film phases and structures. The Hall effect test system (Accent Optical Technology's HL5550) was used to measure the electrical properties of the films, respectively. XPS was measured on a PHI-5000 Versa probe with  $\text{Al K}_\alpha$  radiation with the energy of 1486.6 eV. The step width of the energy channels was set to 0.2 eV. The base pressure of the UHV analysis chamber was  $1 \times 10^{-6}$  Pa. An atomic force microscope (Bruker

Dimension Icon) and KPFM measurements were carried out via the peak force tapping mode, and a map of the contact potential difference was provided. The microstructures were characterized using a transmission electron microscope (FEI Talos-F200S) operated at 200 kV and a high-resolution field-emission transmission electron microscope. The sample preparation has been performed by a dual beam FIB microscope, Strata 400S (FEI). The sample was mounted on a Mo TEM grid and milled down to an 80 nm thin lamella. An SEM with an acceleration voltage of 15 kV was used to observe and record the film morphologies. The lifetimes of carriers were measured by time-resolved photoluminescence spectroscopy at room temperature. The TRPL spectroscopy measurements of the devices were carried out to measure lifetimes of carriers at room temperature with an optical spectrometer (SP-2500, Princeton Instruments) with excitation wavelengths of 532 and 808 nm.

The current density–voltage ( $J$ – $V$ ) characteristics of solar cells were measured using a solar simulator calibrated with a certified Si solar cell under AM1.5G standard conditions ( $1000 \text{ W m}^{-2}$  and  $25^\circ\text{C}$ ). The EQE spectra were acquired using a chopped white light source calibrated with a certified Si solar cell and an InGaAs solar cell. The  $C$ – $V$  (using a direct current bias of  $0.5 \text{ V} \approx -1.0 \text{ V}$  and an alternating current excitation source of  $50 \text{ mV}$  at  $100 \text{ kHz}$  in the dark) and AS measurements were performed with an HP 4284A LCR meter. EIS spectra were measured using an Autolab PGSTAT302N (Metrohm Autolab, The Netherlands) electrochemical workstation in the dark, scanning from  $10 \text{ Hz}$  to  $2 \text{ MHz}$  under  $50 \text{ mV}$  bias.

## Supporting Information

Supporting Information is available from the Wiley Online Library or from the author.

## Acknowledgements

This work was supported by the National Key R&D Program of China (2019YFB1503500), the Natural Science Foundation of China (U1902218, 11774187), the 111 project (B16027), and the Fundamental Research Funds for the Central Universities Nankai University (632111103). The authors would like to thank Shiyanjia Lab (www.shiyanjia.com) for the support of TEM testing.

## Conflict of Interest

The authors declare no conflict of interest.

## Data Availability Statement

Research data are not shared.

## Keywords

Ag doping, gradient energy band, kesterite, surface inversion

Received: June 6, 2021

Revised: August 25, 2021

Published online: October 8, 2021

- [1] W. Wang, M. T. Winkler, O. Gunawan, T. Gokmen, T. K. Todorov, Y. Zhu, D. B. Mitzi, *Adv. Energy Mater.* **2014**, *4*, 1301465.
- [2] D.-H. Son, S.-H. Kim, S.-Y. Kim, Y.-I. Kim, J.-H. Sim, S.-N. Park, D.-H. Jeon, D.-K. Hwang, S.-J. Sung, J.-K. Kang, K.-J. Yang, D.-H. Kim, *J. Mater. Chem. A* **2019**, *7*, 25279.

- [3] M. Nakamura, K. Yamaguchi, Y. Kimoto, Y. Yasaki, T. Kato, H. Sugimoto, *IEEE J. Photovoltaics* **2019**, *9*, 1863.
- [4] Y. Gong, Y. Zhang, Q. Zhu, Y. Zhou, R. Qiu, C. Niu, W. Yan, W. Huang, H. Xin, *Energy Environ. Sci.* **2021**, *14*, 2369.
- [5] Y. Qi, Q. Tian, Y. Meng, D. Kou, Z.-J. Zhou, W.-H. Zhou, S. Wu, *ACS Appl. Mater. Interfaces* **2017**, *9*, 21243.
- [6] Z. Su, G. Liang, P. Fan, J. Luo, Z. Zheng, Z. Xie, W. Wang, S. Chen, J. Hu, Y. Wei, C. Yan, J. Huang, X. Hao, F. Liu, *Adv. Mater.* **2020**, *32*, 2000121.
- [7] A. Cabas-Vidani, S. G. Haass, C. Andres, R. Caballero, R. Figi, C. Schreiner, J. A. Márquez, C. Hages, T. Unold, D. Bleiner, A. N. Tiwari, Y. E. Romanyuk, *Adv. Energy Mater.* **2018**, *8*, 1801191.
- [8] J. Li, D. Wang, X. Li, Y. Zeng, Y. Zhang, *Adv. Sci.* **2018**, *5*, 1700744.
- [9] X. Li, Z. Hou, S. Gao, Y. Zeng, J. Ao, Z. Zhou, B. Da, W. Liu, Y. Sun, Y. Zhang, *Sol. RRL* **2018**, *2*, 1800198.
- [10] Z. Su, J. M. R. Tan, X. Li, X. Zeng, S. K. Batabyal, L. H. Wong, *Adv. Energy Mater.* **2015**, *5*, 1500682.
- [11] H. Guo, G. Wang, R. Meng, Y. Sun, S. Wang, S. Zhang, J. Wu, L. Wu, G. Liang, H. Li, Y. Zhang, *J. Mater. Chem. A* **2020**, *8*, 22065.
- [12] D. Wang, J. Wu, X. Liu, L. Wu, J. Ao, W. Liu, Y. Sun, Y. Zhang, *J. Energy Chem.* **2019**, *35*, 188.
- [13] Z. Yuan, S. Chen, H. Xiang, X.-G. Gong, A. Walsh, J.-S. Park, I. Repins, S. Wei, *Adv. Funct. Mater.* **2015**, *25*, 6733.
- [14] H. Cui, C.-Y. Lee, W. Li, X. Liu, X. Wen, X. Hao, *Int. J. Photoenergy* **2015**, *2015*, 170507.
- [15] T. Gershon, Y. S. Lee, P. Antunez, R. Mankad, S. Singh, D. Bishop, O. Gunawan, M. Hopstaken, R. Haight, *Adv. Energy Mater.* **2016**, *6*, 1502468.
- [16] Y. Wu, Y. Sui, W. He, F. Zeng, Z. Wang, F. Wang, B. Yao, L. Yang, *Nanomaterials* **2020**, *10*, 96.
- [17] C. J. Hages, M. J. Koeper, R. Agrawal, *Sol. Energy Mater. Sol. Cells* **2016**, *145*, 342.
- [18] H. Deng, J. Luo, S. Li, S. Wei, *Phys. Rev. Lett.* **2016**, *117*, 165901.
- [19] T. Gershon, K. Sardashti, O. Gunawan, R. Mankad, S. Singh, Y. S. Lee, J. A. Ott, A. Kummel, R. Haight, *Adv. Energy Mater.* **2016**, *6*, 1601182.
- [20] C. Xiao, C.-S. Jiang, H. Moutinho, D. Levi, Y. Yan, B. Gorman, M. Al-Jassim, *Prog. Photovoltaics* **2017**, *25*, 33.
- [21] J. Kavalakatt, D. Abou-Ras, J. Haarstrich, C. Ronning, M. Nichterwitz, R. Caballero, T. Rissom, T. Unold, R. Scheer, H. W. Schock, *J. Appl. Phys.* **2014**, *115*, 014504.
- [22] Y. Sun, L. Du, Z. Liu, W. Ding, C. Gao, W. Yu, *Mater. Lett.* **2017**, *195*, 76.
- [23] J. Li, H. Wang, M. Luo, J. Tang, C. Chen, W. Liu, F. Liu, Y. Sun, J. Han, Y. Zhang, *Sol. Energy Mater. Sol. Cells* **2016**, *149*, 242.
- [24] S. Gao, Y. Zhang, J. Ao, S. Lin, Z. Zhang, X. Li, D. Wang, Z. Zhou, G. Sun, F. Liu, Y. Sun, *Sol. Energy Mater. Sol. Cells* **2018**, *176*, 302.
- [25] W. Gong, T. Tabata, K. Takei, M. Morihama, T. Maeda, T. Wada, *Phys. Status solidi c* **2015**, *12*, 700.
- [26] J. Márquez, M. Neuschitzer, M. Dimitrievska, R. Gunder, S. Haass, M. Werner, Y. E. Romanyuk, S. Schorr, N. M. Pearsall, I. Forbes, *Sol. Energy Mater. Sol. Cells* **2016**, *144*, 579.
- [27] J. Li, S. Kim, D. Nam, X. Liu, J. Kim, H. Cheong, W. Liu, H. Li, Y. Sun, Y. Zhang, *Sol. Energy Mater. Sol. Cells* **2017**, *159*, 447.
- [28] M. Dimitrievska, A. Fairbrother, E. Saucedo, A. Pérez-Rodríguez, V. Izquierdo-Roca, *Appl. Phys. Lett.* **2015**, *106*, 073903.
- [29] Y. Sun, P. Qiu, S. Wang, H. Guo, R. Meng, X. Zhou, L. Wu, W. Yu, J. Ao, Y. Zhang, *Sol. RRL* **2021**, *5*, 2100181.
- [30] S. Chen, A. Walsh, X.-G. Gong, S.-H. Wei, *Adv. Mater.* **2013**, *25*, 1522.
- [31] J. Li, Y. Huang, J. Huang, G. Liang, Y. Zhang, G. Rey, F. Guo, Z. Su, X. You, H. Zhu, L. Cai, K. Sun, Y. Sun, S. Chen, X. Hao, Y. Mai, M. A. Green, *Adv. Mater.* **2020**, *32*, 2005268.
- [32] M. Dimitrievska, A. Fairbrother, R. Gunder, G. Gurieva, H. Xie, E. Saucedo, A. Pérez-Rodríguez, V. Izquierdo-Roca, S. Schorr, *Phys. Chem. Chem. Phys.* **2016**, *18*, 8692.

- [33] S. Wang, S. Gao, D. Wang, Z. Jiang, J. Ao, Z. Zhou, S. Liu, Y. Sun, Y. Zhang, *Sol. RRL* **2019**, 3, 1800236.
- [34] J. Park, J. Huang, J. Yun, F. Liu, Z. Ouyang, H. Sun, C. Yan, K. Sun, K. Kim, J. Seidel, S. Chen, M. A. Green, X. Hao, *Adv. Energy Mater.* **2018**, 8, 1701940.
- [35] Z. Zhang, Q. Gao, J. Guo, Y. Zhang, Y. Han, J. Ao, M.-J. Jeng, F. Liu, W. Liu, Y. Zhang, *Sol. RRL* **2020**, 4, 2000059.
- [36] K.-J. Yang, J.-H. Sim, D.-H. Son, D.-H. Kim, G. Y. Kim, W. Jo, S. Song, J. Kim, D. Nam, H. Cheong, J.-K. Kang, *Prog. Photovoltaics* **2015**, 23, 1771.
- [37] G. Y. Kim, A. R. Jeong, J. R. Kim, W. Jo, D.-H. Son, D.-H. Kim, J.-K. Kang, *Sol. Energy Mater. Sol. Cells* **2014**, 127, 129.
- [38] M. Vishwakarma, D. Varandani, C. Andres, Y. E. Romanyuk, S. G. Haass, A. N. Tiwari, B. R. Mehta, *Sol. Energy Mater. Sol. Cells* **2018**, 183, 34.
- [39] S. Gupta, Y. Batra, B. R. Mehta, V. R. Satsangi, *Nanotechnology* **2013**, 24, 255703.
- [40] R. Haerle, E. Riedo, A. Pasquarello, A. Baldereschi, *Phys. Rev. B* **2001**, 65, 0451010.
- [41] M. Ristova, M. Ristov, *Appl. Surf. Sci.* **2001**, 181, 68.
- [42] Y. Sun, H. Guo, P. Qiu, S. Zhang, S. Wang, L. Wu, J. Ao, Y. Zhang, *J. Energy Chem.* **2021**, 57, 618.
- [43] K. Wei, G. S. Nolas, *ACS Appl. Mater. Interfaces* **2015**, 7, 9752.
- [44] B. Zhang, L. Han, S. Ying, Y. Li, B. Yao, *RSC Adv.* **2018**, 8, 19213.
- [45] W.-W. Hsu, J. Y. Chen, T.-H. Cheng, S. C. Lu, W.-S. Ho, Y.-Y. Chen, Y.-J. Chien, C. W. Liu, *Appl. Phys. Lett.* **2012**, 100, 023508.
- [46] W. Shockley, H. J. Queisser, *J. Appl. Phys.* **1961**, 32, 510.
- [47] S. Giraldo, Z. Jehl, M. Placidi, V. Izquierdo-Roca, A. Pérez-Rodríguez, E. Saucedo, *Adv. Mater.* **2019**, 31, 1806692.
- [48] A. D. Collord, H. W. Hillhouse, *Chem. Mater.* **2016**, 28, 2067.
- [49] C. Yan, J. Huang, K. Sun, S. Johnston, Y. Zhang, H. Sun, A. Pu, M. He, F. Liu, K. Eder, L. Yang, J. M. Cairney, N. J. Ekins-Daukes, Z. Hameiri, J. A. Stride, S. Chen, M. A. Green, X. Hao, *Nat. Energy* **2018**, 3, 764.
- [50] T. Walter, R. Herberholz, C. Müller, H. W. Schock, *J. Appl. Phys.* **1996**, 80, 4411.
- [51] S. Chen, J.-H. Yang, X. G. Gong, A. Walsh, S.-H. Wei, *Phys. Rev. B* **2010**, 81, 245204.
- [52] D. Han, Y. Y. Sun, J. Bang, Y. Y. Zhang, H.-B. Sun, X.-B. Li, S. B. Zhang, *Phys. Rev. B* **2013**, 87, 155206.
- [53] J. Li, J. Huang, Y. Huang, H. Tampo, T. Sakurai, C. Chen, K. Sun, C. Yan, X. Cui, Y. Mai, X. Hao, *Sol. RRL* 2100418, <https://doi.org/10.1002/solr.202100418>.
- [54] D. B. Mitzi, O. Gunawan, T. K. Todorov, K. Wang, S. Guha, *Sol. Energy Mater. Sol. Cells* **2011**, 95, 1421.
- [55] T. K. Todorov, J. Tang, S. Bag, O. Gunawan, T. Gokmen, Y. Zhu, D. B. Mitzi, *Adv. Energy Mater.* **2013**, 3, 34.
- [56] J. Li, Y. Zhang, W. Zhao, D. Nam, H. Cheong, L. Wu, Z. Zhou, Y. Su, *Adv. Energy Mater.* **2015**, 5, 1402178.